Inorganic Chemistry

pubs.acs.org/IC

Article

Original Network of Zigzag Chains in the β Polymorph of Fe_2WO_6: Crystal Structure and Magnetic Ordering

Stéphane Caubergh, Nami Matsubara, Françoise Damay, Antoine Maignan, François Fauth, Pascal Manuel, Dmitry D. Khalyavin, Bénédicte Vertruyen,* and Christine Martin

Cite This: https://dx.doi.org/10.1021/acs.inorgchem.0c01024

Read Online

ACCESS | Metrics & More | Article Recommendations | Supporting Information

ABSTRACT: The structural and physical properties of the β polymorph of iron tungstate Fe_2WO_6 have been investigated by synchrotron and neutron diffraction vs temperature, combined with magnetization and dielectric properties measurements. The monoclinic $P2_1/a$ crystal structure of β-Fe_2WO_6 has been determined and consists of an original network of zigzag chains of FeO_6 and WO_6 octahedra sharing trans and skew edges, connected through corners into a 3D structure. Magnetization measurements indicate an antiferromagnetic transition at T_N = 264 K, which corresponds to a ↑↑↓↓ nearly collinear ordering of iron moments inside sequences of four edge-sharing FeO_6 octahedra, as determined by neutron diffraction. A canting of the moments out of the *ac* plane is observed below 150 K, leading to a noncollinear antiferromagnetic structure, the $P2_1/a'$ magnetic space group remaining unchanged. These results are discussed in comparison with the crystal and magnetic structures of γ-Fe_2WO_6 and with the magnetic couplings in other iron tungstates and trirutile Fe_2TeO_6.

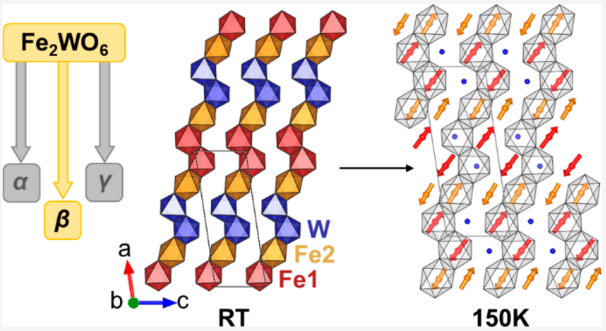

INTRODUCTION

The iron−tungsten−oxygen system has recently been the subject of considerable interest, particularly in the search for iron-based oxide semiconductors for photoelectrochemical applications.[1−3] Within this family, Fe_2WO_6 (in which iron is trivalent) was investigated, for instance, as a photocatalyst to achieve the degradation of organic pollutants in wastewater or the selective reduction of NO_x or as a photoanode for water oxidation.[4−6] Another interesting feature of Fe_2WO_6 is the existence of three polymorphs. Most of the literature concerns the so-called γ-Fe_2WO_6, synthesized by Kozmanov[7] in 1957. Senegas and Galy[8] described the orthorhombic structure of this γ polymorph as a tri-α-PbO_2 cell, which is typically obtained by a solid-state reaction at 900 °C or above. Its magnetic ordering is characterized by the existence of a weak ferromagnetic component,[9,10] and its magnetodielectric properties were recently investigated.[11] Parant et al.[12] showed that a second polymorph, called α-Fe_2WO_6, exists at temperatures as low as 800 °C. This low-temperature phase was described as a columbite structure, another superlattice variant of the α-PbO_2 cell. Literature on the physical properties of this polymorph is scarce.[13,14] In 1992, Walczak et al.[15] obtained a third polymorph, called β-Fe_2WO_6, through long heat treatment between 750 and 840 °C. Its monoclinic structure was not solved at the time. The only published investigation of the physical properties of β-Fe_2WO_6, conducted by Guskos et al.[13] using EPR and bulk magnetic measurements, reported a magnetic transition slightly below room temperature, around 260 K, similar to the case of the α and γ polymorphs. To this day, experimental data dealing with the crystal structure and the macroscopic properties of β-Fe_2WO_6 have remained largely unavailable, most likely because the synthesis of β-Fe_2WO_6 requires very long heat treatment and a single-phase material cannot be obtained easily.[15]

In this article, we report on the synthesis of single-phase β-Fe_2WO_6 and its characterization by high-angular-resolution synchrotron X-ray and neutron powder diffraction and the measurement of bulk magnetic and dielectric properties. An original crystal structure is evidenced, in which the alternation of trans- and skew-edge-sharing octahedra creates sequences of four edge-sharing FeO_6 octahedra, with a nearly collinear up−up−down−down magnetic configuration below 264 K. Below 150 K, a reorientation of the moments outside the *ac* plane leads to noncollinear antiferromagnetic ordering with a small component along the *b* axis. The discussion involves a comparison between the crystal and magnetic structures of the different Fe_2WO_6 polymorphs and considers the magnetic

Received: April 7, 2020

Table 1. Cell Parameters and Crystallographic Parameters of β-Fe_2WO_6 at Room Temperature (R_{Bragg} = 3.55%) and 10 K (R_{Bragg} = 4.43%), Obtained by Simultaneously Using SXRPD and HRNPD Data at RT and SXRPD Data Only at 10 K[a]

RT					10 K				
a (Å)			15.09245(8)		a (Å)			15.06343(4)	
b (Å)			4.59451(2)		b (Å)			4.58614(1)	
c (Å)			5.59628(3)		c (Å)			5.58757(1)	
β (deg)			98.5360(5)		β (deg)			98.5791(2)	
V (Å^3)			383.761(1)		V (Å^3)			381.687(1)	
RT					10 K				
atom	x	y	z	B_{iso} (Å^2)	atom	x	y	z	B_{iso} (Å^2)
W	0.5876(1)	−0.004(1)	0.3613(3)	0.22(1)	W	0.5877(1)	0.0058(4)	0.3617(1)	0.20(1)
Fe1	0.0853(2)	0.008(1)	0.8549(6)	0.63(6)	Fe1	0.0857(2)	0.000(2)	0.8551(4)	0.15(3)
Fe2	0.2551(2)	−0.004(2)	0.2292(6)	0.70(7)	Fe2	0.2548(2)	−0.004(2)	0.2284(4)	0.17(3)
O1	0.9686(6)	−0.243(2)	0.868(1)	1.05(8)	O1	0.970(1)	−0.234(3)	0.862(2)	0.41(8)
O2	0.6890(5)	0.231(2)	0.464(1)	1.05(8)	O2	0.6899(9)	0.227(3)	0.447(2)	0.41(8)
O3	0.6328(5)	−0.226(1)	0.665(1)	0.8(2)	O3	0.637(1)	−0.219(3)	0.670(2)	0.41(8)
O4	0.5240(6)	0.219(1)	−0.371(1)	0.9(2)	O4	0.526(1)	0.217(3)	−0.383(2)	0.41(8)
O5	−0.1365(6)	0.233(2)	0.821(1)	1.05(8)	O5	−0.131(1)	0.236(3)	0.841(3)	0.41(8)
O6	0.6945(5)	0.300(1)	0.948(1)	1.05(8)	O6	0.6966(9)	0.295(3)	0.953(3)	0.41(8)

[a]All atoms stand on general Wyckoff positions (4e) of the $P2_1/a$ space group.

Table 2. Selected Interatomic Distances (in Å) in β-Fe_2WO_6 Corresponding to the Crystallographic Parameters of Table 1.[a]

cation	O	RT	10 K	cation	O	RT	10 K
W	O1	1.866(8)	1.869(13)	Fe1	O1	2.143(9)	2.162(14)
	O2	1.890(8)	1.875(13)		O1	2.118(10)	2.049(15)
	O3	2.012(8)	2.057(12)		O3	1.887(9)	1.887(14)
	O4	2.152(8)	2.046(14)		O4	1.918(8)	1.967(13)
	O4	1.962(9)	2.029(15)		O5	2.168(8)	2.000(13)
	O5	1.810(9)	1.883(13)		O6	1.872(8)	1.933(14)
WO_6	$\langle d \rangle$	1.949(3)	1.960(5)	$Fe1O_6$	$\langle d \rangle$	2.018(4)	2.000(6)
	$\Delta d \times 10^{-4}$	32.9(1)	18.6(1)		$\Delta d \times 10^{-4}$	39.6(1)	19.6(1)
Fe1−Fe1 (intrachain)		3.243(7)	3.254(7)	Fe2	O2	2.077(8)	2.136(12)
Fe1−Fe2 (intrachain)		3.060(5)	3.040(4)		O2	2.165(9)	2.089(14)
Fe2−W (intrachain)		3.045(4)	3.044(3)		O3	2.008(8)	1.943(14)
W−W (intrachain)		3.259(4)	3.251(2)		O5	2.059(10)	2.151(14)
Fe1−Fe2 (interchains)		3.451(8)	3.429(9)		O6	1.907(9)	1.872(16)
Fe2−Fe2 (interchains)		3.430(5)	3.419(4)		O6	1.940(8)	1.910(16)
Fe1−Fe2 (interchains)		3.372(7)	3.378(9)	$Fe2O_6$	$\langle d \rangle$	2.026(4)	2.017(6)
Fe1−W (interchains)		3.516(6)	3.561(6)		$\Delta d \times 10^{-4}$	18.2(1)	30.8(1)

[a]$\langle d \rangle$ is the average bond length (in Å) in MO_6 octahedra (M = W, Fe1, Fe2) and Δd is the distortion parameter calculated for each MO_6 octahedron as $\Delta d = (1/6)\sum_{n=1,6}\{(d_n - \langle d \rangle)/\langle d \rangle\}^2$, with $\langle d \rangle$ being the average M−O distance.

couplings in other motifs of edge-sharing FeO_6 octahedra such as the dimers in trirutile Fe_2TeO_6.

EXPERIMENTAL SECTION

Synthesis and Preliminary Characterizations. Polycrystalline samples of β-Fe_2WO_6 were prepared by a solid-state reaction between α-Fe_2O_3 and WO_3. Commercial iron oxide (α-Fe_2O_3, 99.9%) and tungsten trioxide (WO_3, 99.8%) were both purchased from Alfa-Aesar. The precursor powders were weighed in a Fe/W = 2 ratio and mixed in an agate mortar. The powder mixture was then pressed with a uniaxial press in the shape of bars (2 × 2 × 12 mm). During preliminary experiments, trial preparation conditions taken from Walczak et al.[15] were adjusted by monitoring the evolution of the synthesis with ex situ X-ray diffraction. Brownish black single-phase β-Fe_2WO_6 was obtained by sintering at 850 °C for 21 days in air, with intermediate grinding and pelletizing steps after 7 and 14 days.

Sample quality was checked by room-temperature (RT) X-ray powder diffraction (XRPD), using a Panalytical Xpert Pro diffractometer (Co Kα radiation). The Fe/W stoichiometry was determined by inductively coupled plasma−optical emission spectroscopy (ICP-OES) using an Agilent ICP-OES spectrometer. β-Fe_2WO_6 was dissolved in fuming hydrochloric acid (37 wt %, Acros, for analysis) overnight at 60 °C. Standard solutions of iron and tungsten were prepared by dilution of the respective standard solutions (Merck, traceable to SRM from the NIST). The calibration curves were in the 10−100 mg L^{-1} range. The Fe/W ratio of 2.03 ± 0.03 (confidence interval of ±2 standard deviations) is in good agreement with the Rietveld refinements of synchrotron data at RT indicating a content in hematite of about 0.4% wt % (1 mol %).

Synchrotron X-ray and Neutron Powder Diffraction. Synchrotron X-ray powder diffraction (SXRPD) experiments were performed on the BL04-MSPD beamline of the ALBA synchrotron.[16] Data were collected using a high-intensity-mode detection setup (position-sensitive detector MYTHEN), at the wavelength λ = 0.4427 Å, with the sample enclosed in a spinning glass capillary (0.3 mm inner diameter) at 295 K and in the low-temperature He flow Dynaflow cryostat at 10 K.[17]

https://dx.doi.org/10.1021/acs.inorgchem.0c01024
Inorg. Chem. XXXX, XXX, XXX−XXX

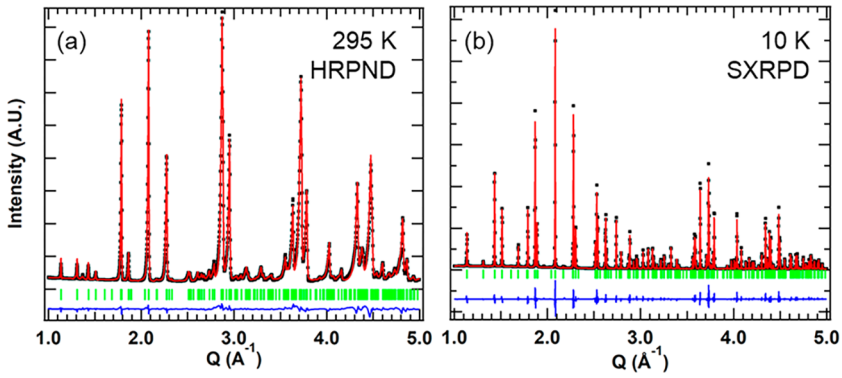

Figure 1. Rietveld refinements of β-Fe_2WO_6: (a) HRNPD data at 295 K; (b) SXRPD data at 10 K. Experimental data are given as black dots, calculated data as a red continuous line, and Bragg reflections as green vertical marks. The difference between the experimental and calculated profiles is displayed at the bottom of the graph as a blue continuous line.

High-resolution neutron powder diffraction (HRNPD) data were collected at 295 K on the WISH time-of-flight (TOF) diffractometer at the ISIS neutron source.[18] The sample was loaded into a 6 mm diameter cylindrical vanadium can and mounted in a cryostat.

Neutron powder diffraction (NPD) data were collected in the temperature range 1.5−300 K at LLB-Orphée on the G4.1 diffractometer (λ = 2.427 Å). The sample was loaded into a 10 mm diameter cylindrical vanadium can.

Structure Refinements. Possible sets of crystal systems and cell parameters were determined using both TREOR[19] and Dicvol[20] programs from SXRPD data collected at 295 K. Atomic positions were determined by the charge-flipping method using Superflip[21] with the JANA2006 program.[22] Refinements of the crystal and magnetic structures and symmetry analysis (magnetic irreducible representation calculations) were performed using the FullProf suite.[23] HRNPD data collected on banks 2−9 were included in the Rietveld calculations. A convolution pseudo-Voigt with back to back exponential functions was employed to model the peak shapes. The scattering angles for the different detector banks are as follows: banks 2/9, 58°; banks 3/8, 90°; banks 4/7, 122°; banks 5/6, 153°.

Magnetic and Electrical Properties. Magnetic characterizations were performed using a SQUID magnetometer (Quantum Design) for zero-field-cooled warming (*zfcw*) and field-cooled warming (*fcw*) measurements from 5 to 300 K in a magnetic field of 100 Oe and for isothermal magnetic field dependent measurements up to 50000 Oe at 5, 25, 50, and 100 K.

For dielectric measurements, a 3.52 × 2.62 × 0.74 mm sample was prepared and silver paste was deposited on the two larger surfaces to attach electric copper wires. The sample was soldered to a homemade sample probe which was inserted in a 14 T-PPMS instrument (Quantum Design). The dielectric permittivity was obtained using an Agilent 4284A LCR meter.

RESULTS

Room-Temperature Structural Investigation of β-Fe_2WO_6. The SXRPD pattern of β-Fe_2WO_6 is indexed with a monoclinic unit cell whose space group is $P2_1/a$ (No. 14) with $a \approx 15.092$ Å, $b \approx 4.594$ Å, $c \approx 5.596$ Å, and $\beta \approx 98.54°$. The crystallographic parameters obtained by combined refinements using SXRPD and HRNPD data and the corresponding interatomic distances are presented in Tables 1 and 2, respectively. Figure 1a shows RT HRPND experimental and calculated patterns, and the corresponding crystal structure is shown in Figure 2.

The three cations (Fe1, Fe2, and W) are in octahedral oxygen environments. The structure can be described as the stacking, along the *b* axis, of layers made of zigzag chains of edge-sharing octahedra (Figure 2a,b). The connectivity between edge-sharing octahedra is conveniently described

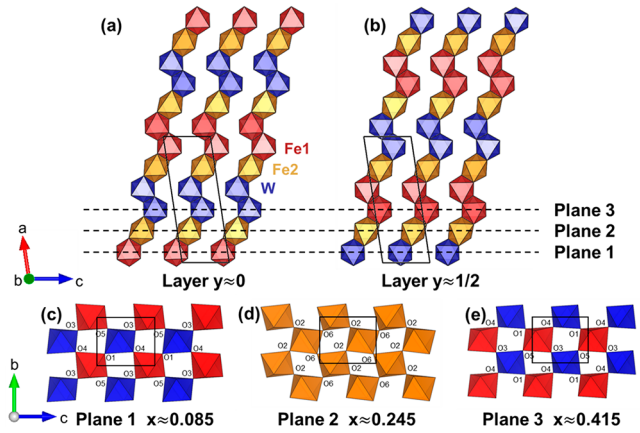

Figure 2. β-Fe_2WO_6 crystal structure: (a, b) projections along [010] showing the zigzag patterns in the two types of layers ($y \approx 0$, 1/2); (c−e) corner-sharing octahedra in the three types of *bc* planes. Color scheme: WO_6 octahedra, blue; $Fe1O_6$ octahedra, red; $Fe2O_6$ octahedra, orange.

using the skew/trans nomenclature[24] (Figure S1). In each zigzag chain, the sequence of cations is Fe1−Fe2−W−W−Fe2−Fe1. $Fe2O_6$ octahedra are sharing trans edges with $Fe1O_6$ and WO_6 octahedra, thus making a linear fragment of three octahedra. Linear fragments are connected to each other into zigzag chains by sharing skew edges: WO_6 octahedra share skew edges with WO_6 and $Fe2O_6$ octahedra, while $Fe1O_6$ octahedra share skew edges with $Fe1O_6$ and $Fe2O_6$. The sequence of cations is identical in the first ($y \approx 0$) and second ($y \approx 1/2$) layers, the zigzag chains being translated by a vector (1/2, 1/2, 1/2) from one layer to the other.

Layers are connected to each other through corner sharing, as illustrated in Figure 2c−e, leading to three kinds of *bc* planes. Two of them consist of alternating $Fe1O_6$ and WO_6 (planes labeled 1 and 3 in Figure 2), and the other is made of $Fe2O_6$ alone (plane 2 in Figure 2).

All octahedra are distorted (Table 2 and Figure S2), with a noticeable off-centering of Fe and W cations (Table S1); there are three long and three short distances, in the ranges 2.118−2.168 and 1.872−1.918 Å, respectively, in $Fe1O_6$ and in the ranges 2.059−2.165 and 1.907−2.008 Å, respectively, in $Fe2O_6$. The average Fe−O and W−O distances in each octahedron are in agreement with the Shannon ionic radii[25] and are very similar to those reported for the γ polymorph.[8]

https://dx.doi.org/10.1021/acs.inorgchem.0c01024
Inorg. Chem. XXXX, XXX, XXX−XXX

Low-Temperature Structural Investigation of β-Fe_2WO_6. SXRPD and NPD data show that β-Fe_2WO_6 does not undergo a structural transition between 350 and 1.5 K, as illustrated in Figure 1b by the 10 K SXRPD pattern. The crystallographic parameters and corresponding interatomic distances at 10 K are presented in Tables 1 and 2, respectively, and display only slight variations in comparison to the values at RT. With decreasing temperature, the unit cell parameters *a*, *b*, and *c* decrease by 0.10−0.15%, while the monoclinic angle β becomes slightly larger (0.03%), causing an overall reduction in the unit cell volume by 0.4%, as shown in Figure 3. In a

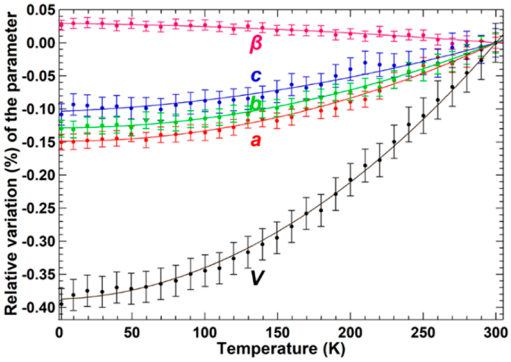

Figure 3. Temperature dependence of the lattice parameters and cell volume of β-Fe_2WO_6 between 1.5 and 300 K, from NPD data (G4.1). Dots are refined values, error bars are taken as ±2 standard deviations, and continuous lines are guides to the eye.

zigzag chain, W atoms in edge-sharing octahedra units get slightly closer to each other at low temperature ($d_{W-W} \approx 3.251$ Å at 10 K vs 3.259 Å at RT). In contrast, Fe1 atoms in edge-sharing octahedra move away from each other, with the Fe1−Fe1 interatomic distance increasing from 3.243 Å at room temperature to 3.254 Å at 10 K.

Investigation of the Magnetic Properties of β-Fe_2WO_6. The magnetic properties of β-Fe_2WO_6 were investigated by a combination of magnetic measurements (Figure 4) and neutron diffraction (Figures 5 and 6). The results are presented and discussed in an integrated manner to analyze the rather complex antiferromagnetic ground state already hinted at in previous reports.[13,14] The transition temperatures T_N and T^* identified in the magnetic susceptibility curves are in good agreement with those taken from neutron diffraction data, taking into account that, over the first few degrees below the magnetic transition, the intensity of magnetic origin is too weak for a reliable refinement.

The magnetic susceptibility curves plotted in Figure 4a evidence a weak variation over the temperature range from RT to 5 K and display a somewhat unusual behavior. When the temperature is decreased from RT, the *zfcw* and *fcw* susceptibility curves are superimposed and increase slowly down to $T_N \approx 264$ K, below which the signal first decreases slightly and then (from 250 K) increases again with a marked split between the *zfcw* and *fcw* curves. The curves feature a small cusp in the *zfcw* data ($T^* \approx 160$ K) with a corresponding change of slope in the *fcw* mode. In addition, the *zfcw* and *fcw* branches both describe a broad downturn around 60 K. The magnetization versus magnetic field curves recorded up to 50000 Oe at 5, 25, and 50, and 100 K (Figure 4b) display a linear behavior and a very small magnetization value of 0.08 μ_B

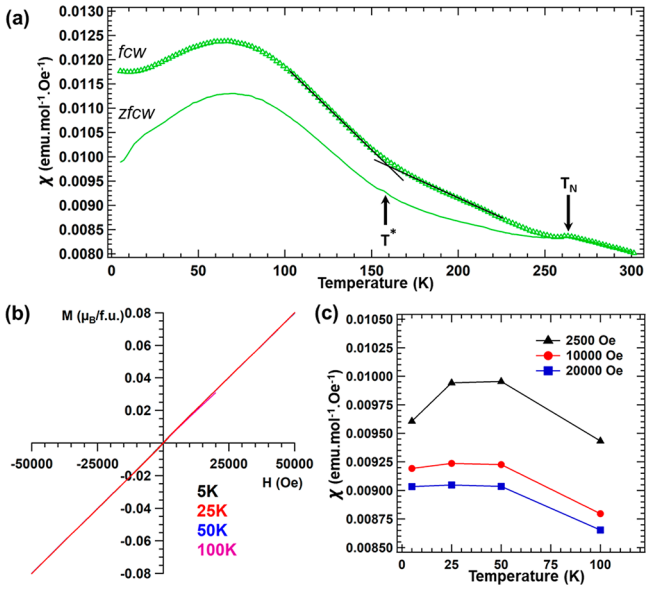

Figure 4. (a) Magnetic susceptibility curves of β-Fe_2WO_6 at 100 Oe as a function of temperature. Black lines are guides to the eye to highlight the change in slope. (b) Field-dependent magnetization curves at 5, 25, 50, and 100 K. (c) Magnetic susceptibility taken at 2500, 10000, and 20000 Oe in the virgin $M(H)$ curves shown in (b).

for 2 Fe(III) at the maximum applied field, supporting predominant antiferromagnetic exchange at low temperature. Nevertheless, the plot of the magnetic susceptibility extracted from the virgin $M(H)$ curves (Figure 4b,c) shows that the smooth bump seen at 60 K at 100 Oe (in the $\chi(T)$ curve of Figure 4a) is suppressed at 20000 Oe. This demonstrates that the interpretation of the $\chi(T)$ curves of β-Fe_2WO_6 is not obvious and that one must be cautious in interpreting their shape. A neutron diffraction investigation was therefore carried out to determine the magnetic structure and its evolution with temperature.

The magnetic transition is also detected in the NPD patterns; an increased intensity is observed below T_N on top of existing Bragg peaks, as illustrated in Figure 5a, around Q = 0.85, 1.3, 1.4, 1.8 $Å^{-1}$. The magnetic structure can therefore be described with the propagation vector $\mathbf{k}$ = (0,0,0). A symmetry analysis performed for the $P2_1/a$ space group with propagation vector $\mathbf{k}$ = (0,0,0) and Wyckoff site 4e yields four possible magnetic irreducible representations (Irrep) of dimension 1, each containing three basis vectors: $\Gamma_{mag} = 3\Gamma_1 \oplus 3\Gamma_2 \oplus 3\Gamma_3 \oplus 3\Gamma_4$. A satisfactory refinement (Figure 5c) in the whole temperature range below T_N is achieved using Γ_2 Irrep, whose basis vectors are given in Table 3.

Below T_N and down to T^*, the best magnetic structure modeling corresponds to magnetic moments on the Fe1 and Fe2 sites confined in the *ac* plane. In each zigzag chain, the Fe spins in the *ac* plane follow a ↑↑↓↓ sequence, each tetramer being separated from the following one by two diamagnetic hexavalent tungsten cations (Figure 6a). The coupling between Fe spins is ferromagnetic for the short Fe1−Fe2 distance (3.040 Å) and antiferromagnetic for the long Fe1−Fe1 distance (3.254 Å). Fe1 and Fe2 are not actually constrained by symmetry to have collinear moments; refining them independently led to the m_x and m_z values given in Figure 5b and Table 4. The observed small misalignment of the spins (a few degrees) is questionable, since the refinement is not significantly improved in comparison to that including

https://dx.doi.org/10.1021/acs.inorgchem.0c01024
Inorg. Chem. XXXX, XXX, XXX−XXX

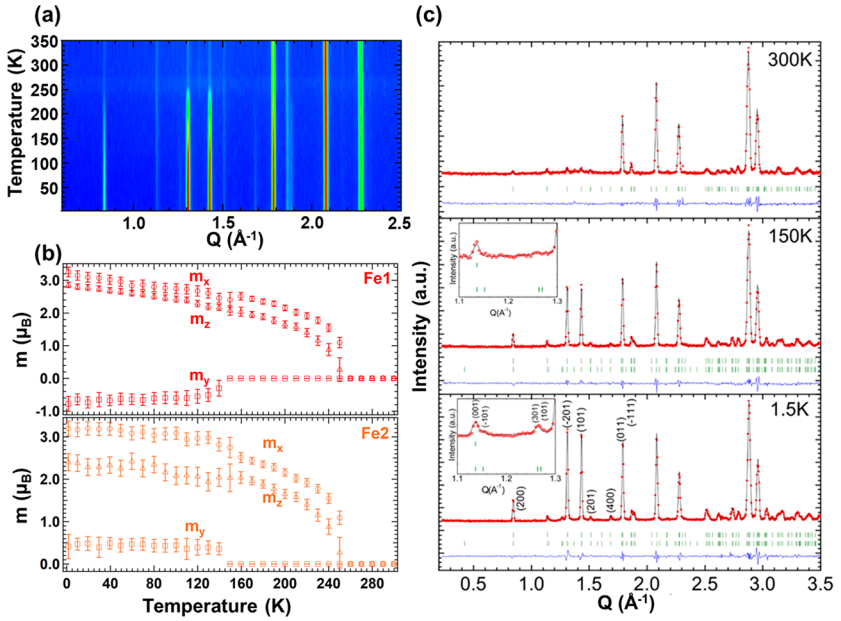

Figure 5. (a) Temperature evolution of NPD (G4.1) patterns of β-Fe_2WO_6. (b) Temperature evolution of the components of the Fe magnetic moments. (c) NPD patterns at 300, 150, and 1.5 K. Experimental data are given as red dots, the calculated profile is given by a black continuous line, and Bragg reflections are shown as green vertical marks. The difference between the experimental and calculated profiles is displayed at the bottom of the graph as a blue continuous line. The insets at 150 and 1.5 K illustrate the increasing magnetic intensity on the (301) Bragg position, indicating a nonzero m_y component of the magnetic moment.

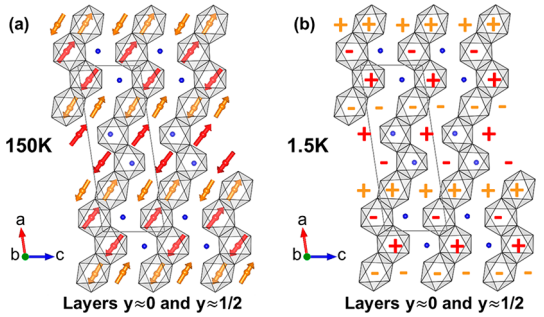

Figure 6. (a) Magnetic structure of β-Fe_2WO_6 at 150 K. The Fe1 and Fe2 moments are confined in the *ac* planes from T_N to T^*. Moments shown in octahedra belong to the $y \approx 0$ layer, while moments shown as isolated arrows belong to the $y \approx 1/2$ layer. (b) Arrangement of the m_y component below T^* (positive (+) and negative (−) signs indicate a positive or a negative m_y component, respectively). This small m_y component is in addition to the magnetic structure given in (a). Color scheme: W, blue; Fe1, red; Fe2, orange.

Table 3. Basis Functions for Axial Vectors Bound to the Wyckoff Site 4e of the $P2_1/a$ Space Group, within the Irreducible Representation Γ_2 (Propagation Vector k = 0,0,0)

Γ_2	(x, y, z)	$(-x + 1/2, y + 1/2, -z + 1/2)$	$(y + 1/2, -x + 1/2, z + 1/2)$	$(y, x, -z + 1)$
ψ_1	1,0,0	−1,0 0	−1,0,0	1,0,0
ψ_2	0,1,0	0,1,0	0,−1,0	0,−1,0
ψ_3	0,0,1	0,0,−1	0,0,−1	0,0,1

constraints between Fe1 and Fe2 moments. However, the evolution of the magnetic susceptibility below T_N (see Figure 4) supports the canting of the AFM structure.

Below T^*, the appearance of a peak at the (301) Bragg position (Figure 5c) indicates the onset of an out-of-plane magnetic component m_y (Figures 5b and Table 4). In contrast with the in-*ac*-plane magnetic order observed at and above T^*, refining the components m_y independently on the two Fe sites led to a much better agreement factor; m_x and m_z were also refined independently for coherence (Figure 5b). The resulting magnetic order is therefore noncollinear with an antiferromagnetic m_y component highlighted in Figure 6b. This reorientation of the spins below T^* is accompanied by an increase in the calculated moment value, which reaches about 4 μ_B for both sites at 1.5 K, noticeably lower than the 5 μ_B value expected for Fe(III) but much higher than the moments of 2.55 and 2.15 μ_B reported in γ-Fe_2WO_6.[10]

Table 4. Magnitude (in μ_B) of the Components of the Magnetic Moments on Fe1 and Fe2 at 150 and 1.5 K

	150 K		1.5 K	
	Fe1	Fe2	Fe1	Fe2
m_x	2.4(2)	2.7(2)	3.2(2)	3.2(2)
m_y	0	0	−0.8(2)	0.4(3)
m_z	2.1(1)	2.0(3)	2.9(1)	2.4(2)
$\lvert m_{TOT} \rvert$	2.9(1)	3.1(1)	4.1(2)	3.7(3)

In summary, the picture of magnetism emerging from the neutron diffraction study and the magnetic curves is as follows: (i) below T_N, there appears an antiferromagnetic structure which is nearly collinear with spins in the *ac* plane; (ii) the small difference in the spin orientation of iron in the two sites (i.e., canting) and their different and low values in comparison to the theoretical value are in agreement with the splitting of the *zfcw* and *fcw* curves; (iii) the cusp observed on the *zfcw* susceptibility curve around T^* corresponds to the spin reorientation inducing a new component along the *b* axis. Since there is no clear change in the NPD data around 60 K (such as an evolution of the background at low angle or in the width of the Bragg peaks in their lower part), the downturn in the susceptibility could be related to a small ferromagnetic-like

https://dx.doi.org/10.1021/acs.inorgchem.0c01024
Inorg. Chem. XXXX, XXX, XXX−XXX

component related to the evolution of the slightly different temperature dependences of the magnetic components of the two iron cations (Figure 5b).

Irrep Γ_2 corresponds to the Shubnikov group $P2_1/a'$ (BNS #14.78), which allows a magnetoelectric (direct effect) tensor. Coherently with the rather low synthesis temperature, leading to a sintering of low quality, the measurements of the dielectric permittivity as a function of temperature (Figure 7) reveal a

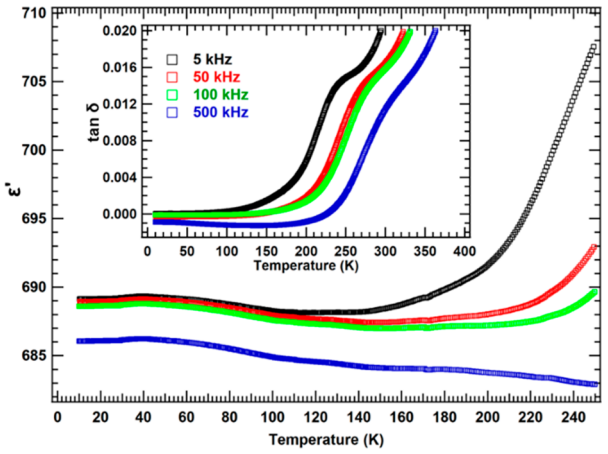

Figure 7. Dielectric permittivity (ε') of β-Fe_2WO_6 as a function of temperature. Inset: dielectric loss (tan δ) as a function of temperature.

leaky behavior, characterized by losses (tan δ) which increase rapidly as the temperature increases above ~120 K and shift toward higher temperatures as the frequency increases. This feature unfortunately hinders the electrical polarization measurements. The same problem of sinterability also precluded measurement of the specific heat capacity, which might have provided valuable insight into the nature of the transitions. However, in the case of a sample of a γ polymorph sintered at 950 °C, the $C_p(T)$ curve reported by Panja et al.[11] between 150 K and RT revealed only a very weak signature in the vicinity of the high-temperature transition.

DISCUSSION

Structural Relationships in Iron Tungstates. As illustrated in Figure 8, the newly solved structure of β-Fe_2WO_6 joins γ-Fe_2WO_6 and Fe(II) tungstate $FeWO_4$ in a group of compounds that can be described as stackings of zigzag chains made of edge-sharing MO_6 octahedra. In polymorph β (Figure 8a), these chains are built from trans- and skew-edge-sharing octahedra; all chains follow the same Fe−Fe−Fe−Fe−W−W sequence and are connected through corners from one layer to the next. Polymorph γ (Figure 8b) crystallizes in the tri-α-PbO_2 structure (*Pbcn*), with zigzag chains of octahedra sharing skew edges.[8] If an ideal ordering of Fe and W cations is assumed, one-third of the zigzag chains in a layer contain $Fe1O_6$ octahedra only while two-thirds of the chains consist of alternating $Fe2O_6$ and WO_6 octahedra. The layers of zigzag chains are stacked along the *a* axis with a displacement of (1/2, 1/2, 0). From one layer to the next, octahedra share corners. $FeWO_4$[26,27] (Figure 8c) presents a monoclinic structure in space group $P2/c$ with a slight monoclinic distortion: β = 90.17°. This structure displays the same zigzag chains as in γ-Fe_2WO_6 but there is no mixing of Fe and W in the chains, and layers of FeO_6 zigzags alternate with layers of WO_6 zigzags.

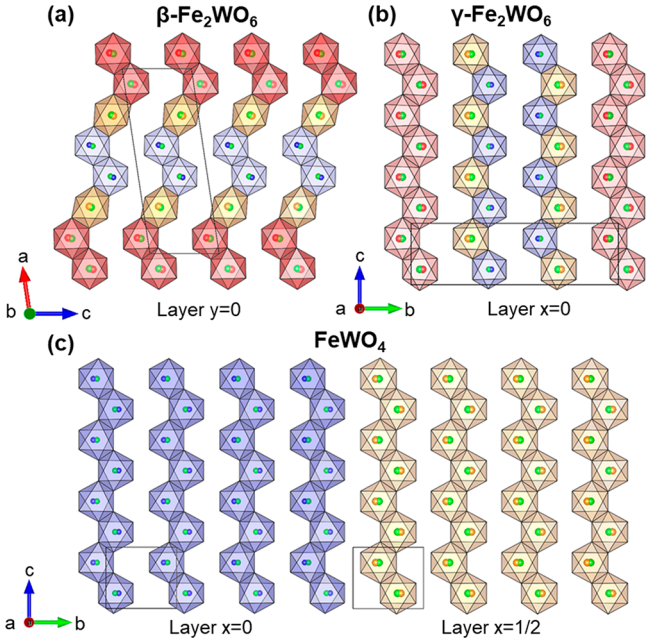

Figure 8. Representations of the structures of (a) β-Fe_2WO_6, (b) γ-Fe_2WO_6, and (c) $FeWO_4$ at room temperature. Color scheme: WO_6 octahedra, blue; $Fe1O_6$ octahedra, red; $Fe2O_6$ octahedra, orange. The off-centering of the cations is evidenced by green spheres indicating the positions of the barycenters.

In all three structures, Fe and W cations are clearly off-centered in their MO_6 octahedra as shown in Figure 8 and Tables S1−S3. Cations in edge-sharing octahedra shift away from each other in a direction roughly perpendicular to the axis of the zigzag chains, except for the Fe2 cations in polymorph β, which by shifting away from their W neighbor move closer to their Fe1 neighbor, due to the trans configuration. The amplitude of off-centering for this Fe2 cation in polymorph β (0.1296 Å along the *c* axis) is smaller than those for Fe1 and W (0.2711 and 0.2531 Å, respectively). Such off-centering seems to be specific to Fe(II) and Fe(III) tungstates, since it is not observed in Fe_2TeO_6[28] but is seen in the ordered aeschynite $RFeWO_6$.[29] Indeed, a majority of the compounds with d^0 W^{6+} in an octahedral coordination display an out-of-center distortion driven by the second-order Jahn−Teller (SOJT) effect.[30−33] In the SOJT effect, the near-degeneracy which is removed by the distortion is that of states created by the mixing of the empty d levels of tungsten with the full 2p levels of the oxygen neighbors. As argued by Kunz and Brown,[31] such a distortion driven by electronic effects is usually supported by an adaptation of the whole structural network, which stabilizes the structure. As a complement to the interatomic distances W−O, Fe1−O, and Fe2−O reported in Table 2 and Figure S2, Figure 9 plots the distance of each oxygen to its three cationic neighbors. In the case of oxygen atoms connected to two Fe and one 1 W, the W−O distance is usually the shortest of the three (except for O3). Oxygen O4, which connects the two tungstens in the W_2O_{10} unit, exhibits two long W−O bond lengths probably due to the repulsion between cations of high oxidation state. In the case of O6 which bonds to three Fe, the Fe^{3+}−O distances are similar to the typical W^{6+}−O distances. This complex pattern of off-centered cations and distorted octahedra results in an adapted structure where the environment of all cations corresponds to a stable situation according

https://dx.doi.org/10.1021/acs.inorgchem.0c01024
Inorg. Chem. XXXX, XXX, XXX−XXX

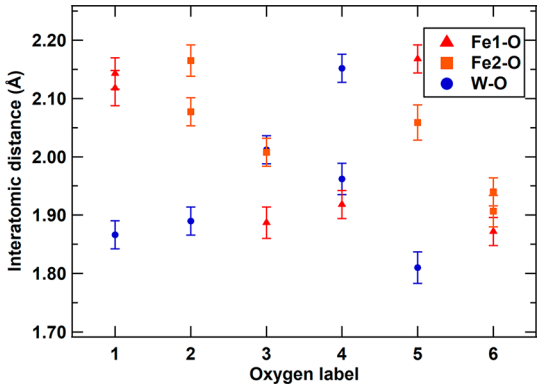

Figure 9. Distribution of the interatomic Fe1 (red ▲)/Fe2 (orange ▼)/W (blue ●)−O distances (y axis) for each of the six oxygen atoms in the structure (x axis). The error bars correspond to 3 times the standard deviations calculated using FullProf.

to Pauling's second rule,[34] as shown by the calculation of charge distribution summarized in Table S4.

Magnetic Networks of Fe(III) and Magnetic Exchange Paths in Fe_2WO_6 Polymorphs. The structural differences between the β and γ polymorphs of Fe_2WO_6 create different networks of magnetic Fe(III) cations, which can be described as follows. In polymorph β, the edge-sharing octahedra in the zigzag chains form (Fe2−Fe1−Fe1−Fe2) zigzag tetramers; the $Fe2O_6$ octahedra at each end of the tetramers share corners with $Fe2O_6$ octahedra of four adjacent tetramers, resulting in planes of corner-sharing $Fe2O_6$ octahedra (plane 2 in Figure 2d). In polymorph γ, the zigzag chains of edge-sharing $Fe1O_6$ are connected through corners to $Fe2O_6$ octahedra; the $Fe2O_6$ octahedra share edges with nonmagnetic WO_6 and are therefore involved in magnetic interactions only through corner sharing with $Fe2O_6$ and $Fe1O_6$ in adjacent chains.

Common to both polymorphs is the presence of Fe(III) cations ($3d^5$): according to the semiempirical Goodenough−Kanamori (GK) rules, $3d^5$−$3d^5$ couplings are expected to be antiferromagnetic in the direct exchange (~90° orbital configuration between edge-sharing octahedra for instance) and superexchange (~180° orbital configuration; e.g., between corner-sharing octahedra) cases. Table 5 summarizes the magnetic couplings (established from the magnetic ground states determined in the present work for β-Fe_2WO_6 and in the study by Pinto et al.[10] for γ-Fe_2WO_6) inside and between the zigzag chains and provides the corresponding values for the Fe−Fe distances and Fe−O−Fe angles. An illustrated version of the same information is available in Figure S3.

In both polymorphs, the magnetic interactions between chains are superexchange mediated (Fe−Fe distances between 3.3 and 3.8 Å, with Fe−O−Fe angles between 125 and 130°) and are always antiferromagnetic, in good agreement with the GK rules.

The description of magnetic couplings within zigzag chains is more complex. In both compounds, the Fe−O−Fe angles in chains are smaller (between 94 and 105°) than those between chains. In polymorph β, coupling within a tetramer in the zigzag chain is ferromagnetic between Fe1 and Fe2 and antiferromagnetic between Fe1 and Fe1, leading to a ↑↑↓↓ magnetic configuration. In polymorph γ, only Fe1 atoms are magnetically coupled through edge-sharing in zigzag chains and the coupling is also ferromagnetic. In both cases, the FM coupling takes place for short Fe−Fe distances (3.04 Å in polymorph β, 3.12 Å in polymorph γ), therefore suggesting a ferromagnetic direct exchange contribution, in contrast to what is expected from the GK rules. The AFM coupling between Fe1 and Fe1 within the tetramers of polymorph β is observed for a longer Fe−Fe distance (3.25 Å). As a comparison, the magnetic network in trirutile Fe_2TeO_6[28] is made of dimer units of two edge-sharing FeO_6 octahedra, connected through corners, with antiferromagnetic coupling even for the shortest Fe−Fe distance (3.03 Å in the dimer: i.e., shorter than the shortest distance in the Fe_2WO_6 polymorphs), in good agreement with the GK rules. Like the results on the $Cr_2Te_{1-x}W_xO_6$ system,[35] this could suggest that another key parameter controlling the sign of direct exchange magnetic interactions is the orbital hybridization between Fe 3d and O 2p orbitals through the 5d W states and therefore is beyond the GK formalism.

The spin orientation in an individual FeO_6 octahedron is another difference between the Fe_2WO_6 polymorphs (Figure 6 and Figure S4). Single-ion magnetic anisotropy, that is, the term in the magnetic energy dependent on the relative direction of the spin with respect to the local octahedral environment, is not easily assessed from structural considerations, since the Fe(4e) site symmetry is 1. In both polymorphs, there are two independent Fe sites in the crystal structure, so that each site could have its own local anisotropy, owing to the strong effect of the local environment on single-ion magnetic anisotropy, even for a d^5 element (L = 0).[36] Figure S4 shows that, in β-Fe_2WO_6, the canting away from the order in the ac plane below 150 K corresponds to a realignment of the spin toward the basal plane of the

Table 5. Magnetic Couplings, Interatomic Fe−Fe Distances, and Fe−O−Fe Angles in Polymorphs β-Fe_2WO_6 (This Work) and γ-Fe_2WO_6[10]

	polymorph β (10 K)		polymorph γ (4.2 K)	
	AFM coupling	FM coupling	AFM coupling	FM coupling
intrachain (edge-sharing octahedra)	Fe1−Fe1: 3.254 Å	Fe1−Fe2: 3.040 Å		Fe1−Fe1: 3.122 Å
	101.0/101.0°	94.1/104.6°		97.1/97.1°
interchains (corner-sharing octahedra)	Fe1−Fe2: 3.378 Å			
	Fe1−Fe2: 3.429 Å		Fe2−Fe2: 3.486 Å	
	Fe2−Fe2: 3.419 Å		Fe1−Fe2: 3.626 Å	
	Fe2−Fe2: 3.822 Å		125.8−126.1°	
	from 125.1 to 129.5°			
around Fe1	3	1	2	2
around Fe2	6	1	6	0

https://dx.doi.org/10.1021/acs.inorgchem.0c01024
Inorg. Chem. XXXX, XXX, XXX−XXX

octahedron, together with an increase in $|m_{TOT}|$ (Table 4). However, at this stage, it is not possible to conclude as to whether the observed spin reorientation is a result of competing magnetic exchanges owing to the complex topology of the magnetic network, if single-ion anisotropy is involved or not or if another scenario altogether is at play. If single crystals could be obtained, inelastic neutron scattering experiments would provide further insight into the details of the relevant parameters (hierarchy of magnetic exchanges, role of single-ion anisotropy in particular) stabilizing the magnetic ground state of β-Fe_2WO_6.

CONCLUSION

The monoclinic polymorph β-Fe_2WO_6 exhibits an original crystal structure, based on the alternation of FeO_6 and WO_6 octahedra sharing trans or skew edges. The corresponding magnetic network is built on Fe(III) tetramers, which order below 264 K in a nearly collinear up−up−down−down configuration in the *ac* plane. These tetramers are coupled antiferromagnetically, the magnetic ordering having the $P2_1/a'$ symmetry. Below 150 K, a reorientation of the Fe(III) moments is observed, which leads to a noncollinear antiferromagnetic order with a small component of the Fe(III) moments along the *b* axis.

This determination of the β polymorph structure unlocks the possibility to use the Fe_2WO_6 $\alpha/\beta/\gamma$ system as a platform to study the mechanisms governing the phase transitions and functional properties in such iron oxides. Further work is underway to build a clearer view of the formation conditions of each polymorph, including through solution-based procedures.

In addition, it is hoped that such synthesis routes would make it possible to prepare different polymorphs with similar characteristics of particle size and surface area, in order to study whether and how the structural differences affect the (photo)catalytic/photoelectrochemical properties. In 2017, Abdi et al.[5] used spray pyrolysis of an alcoholic solution to prepare a 400 nm thick film whose diffractogram displayed broad diffraction peaks at some positions corresponding to a partially ordered γ phase. They assessed the suitability of this film as a candidate photoanode for the oxidation of water and concluded that it was better suited to other photocatalytic applications, especially in environmental remediation. Obviously, if the so-far-untested β polymorph turns out to display promising properties, practical prospects would only be realistic if the heat treatment time is drastically reduced, thanks to the solution synthesis route.

ASSOCIATED CONTENT

Supporting Information

The Supporting Information is available free of charge at https://pubs.acs.org/doi/10.1021/acs.inorgchem.0c01024.

Representations of "skew" and "trans" edges forming a zigzag chain of octahedra, projections along [010] and interatomic distances and angles in β-Fe_2WO_6 at room temperature and 10 K, representations of the environments and magnetic interactions of Fe1 and Fe2 in β-Fe_2WO_6 and γ-Fe_2WO_6 and orientations of the Fe^{3+} moments in the FeO_6 octahedra in β-Fe_2WO_6 and γ-Fe_2WO_6. Atomic positions, barycenter positions, and off-centering in the MO_6 octahedra in polymorph β, polymorph γ, and $FeWO_4$. The formal charge, *q*, of the cations and the charge distribution *Q* calculated for each octahedron with and without off-centering of the cations (PDF)

Accession Codes

CCDC 1995152 and 1995169 contain the supplementary crystallographic data for this paper. These data can be obtained free of charge via www.ccdc.cam.ac.uk/data_request/cif, or by emailing data_request@ccdc.cam.ac.uk, or by contacting The Cambridge Crystallographic Data Centre, 12 Union Road, Cambridge CB2 1EZ, UK; fax: +44 1223 336033.

AUTHOR INFORMATION

Corresponding Author

Bénédicte Vertruyen − *GREENMAT, CESAM Research Unit, Université de Liège, 4000 Liege, Belgium;* orcid.org/0000-0002-0128-7862; Email: b.vertruyen@uliege.be

Authors

Stéphane Caubergh − *GREENMAT, CESAM Research Unit, Université de Liège, 4000 Liege, Belgium;* orcid.org/0000-0003-4284-5549

Nami Matsubara − *CRISMAT, Normandie Univ, ENSICAEN, UNICAEN, CNRS, CRISMAT, 14000 Caen, France; Université Paris-Saclay, CEA-CNRS UMR12, Laboratoire Léon Brillouin, 91191 Gif-sur-Yvette Cedex, France;* orcid.org/0000-0002-8324-710X

Françoise Damay − *Université Paris-Saclay, CEA-CNRS UMR12, Laboratoire Léon Brillouin, 91191 Gif-sur-Yvette Cedex, France*

Antoine Maignan − *CRISMAT, Normandie Univ, ENSICAEN, UNICAEN, CNRS, CRISMAT, 14000 Caen, France;* orcid.org/0000-0002-4157-5367

François Fauth − *ALBA-CELLS Synchrotron, 08290 Barcelona, Spain;* orcid.org/0000-0001-9465-3106

Pascal Manuel − *ISIS Pulsed Neutron Facility, STFC Rutherford Appleton Laboratory, Chilton, Oxfordshire OX11 0QX, United Kingdom*

Dmitry D. Khalyavin − *ISIS Pulsed Neutron Facility, STFC Rutherford Appleton Laboratory, Chilton, Oxfordshire OX11 0QX, United Kingdom*

Christine Martin − *CRISMAT, Normandie Univ, ENSICAEN, UNICAEN, CNRS, CRISMAT, 14000 Caen, France;* orcid.org/0000-0003-1567-5505

Complete contact information is available at: https://pubs.acs.org/10.1021/acs.inorgchem.0c01024

Author Contributions

All authors have given approval to the final version of the manuscript.

Funding

Fonds De La Recherche Scientifique-FNRS, Fonds pour la Formation à la Recherche dans l'Industrie et dans l'Agriculture (FRIA) (Grant No. 5200119F).

Notes

The authors declare no competing financial interest.

ACKNOWLEDGMENTS

S.C. thanks FRIA (Belgium) for a Ph.D. fellowship. S.C. and B.V. are grateful to the University of Liège and FRS-FNRS (Belgium) for travel and equipment grants. This work was partially supported by the IUCr2017-STOE grant, awarded to N.M.

REFERENCES

(1) Bera, S.; Rawal, S. B.; Kim, H. J.; Lee, W. I. Novel Coupled Structures of $FeWO_4/TiO_2$ and $FeWO_4/TiO_2/CdS$ Designed for Highly Efficient Visible-Light Photocatalysis. *ACS Appl. Mater. Interfaces* **2014**, *6* (12), 9654−9663.

(2) Zhou, Y.-X.; Yao, H.-B.; Zhang, Q.; Gong, J.-Y.; Liu, S.-J.; Yu, S.-H. Hierarchical $FeWO_4$ Microcrystals: Solvothermal Synthesis and Their Photocatalytic and Magnetic Properties. *Inorg. Chem.* **2009**, *48* (3), 1082−1090.

(3) Sieber, K.; Leiva, H.; Kourtakis, K.; Kershaw, R.; Dwight, K.; Wold, A. Preparation and Properties of Substituted Iron Tungstates. *J. Solid State Chem.* **1983**, *47* (3), 361−367.

(4) Wang, Y.; Zeng, Y.; Chen, X.; Wang, Q.; Wan, S.; Wang, D.; Cai, W.; Song, F.; Zhang, S.; Zhong, Q. Tailoring Shape and Phase Formation: Rational Synthesis of Single-Phase $BiFeWO_x$ Nano-octahedra and Phase Separated Bi_2WO_6-Fe_2WO_6 Microflower Heterojunctions and Visible Light Photocatalytic Performances. *Chem. Eng. J.* **2018**, *351*, 295−303.

(5) Abdi, F. F.; Chemseddine, A.; Berglund, S. P.; van de Krol, R. Assessing the Suitability of Iron Tungstate (Fe_2WO_6) as a Photoelectrode Material for Water Oxidation. *J. Phys. Chem. C* **2017**, *121* (1), 153−160.

(6) Rawal, S. B.; Ojha, D. P.; Sung, S. Do; Lee, W. I. Fe_2WO_6/TiO_2, an Efficient Visible-Light Photocatalyst Driven by Hole-Transport Mechanism. *Catal. Commun.* **2014**, *56*, 55−59.

(7) Kozmanov, Y. D. Investigation of the High Temperature Oxidation of Some Iron Tungten Alloys. *Zh. Fiz. Khim.* **1957**, *31*, 1861.

(8) Senegas, J.; Galy, J. L'oxyde Double Fe_2WO_6. I. Structure Cristalline et Filiation Structurale. *J. Solid State Chem.* **1974**, *10* (1), 5−11.

(9) Weitzel, H. Magnetische Strukturen von $NiNb_2O_6$ Und Fe_2WO_6. *Acta Crystallogr., Sect. A: Cryst. Phys., Diffr., Theor. Gen. Crystallogr.* **1976**, *32* (4), 592−597.

(10) Pinto, H.; Melamud, M.; Shaked, H. Magnetic Structure of Fe_2WO_6, a Neutron Diffraction Study. *Acta Crystallogr., Sect. A: Cryst. Phys., Diffr., Theor. Gen. Crystallogr.* **1977**, *33* (4), 663−667.

(11) Panja, S. N.; Kumar, J.; Harnagea, L.; Nigam, A. K.; Nair, S. γ-Fe_2WO_6 − A Magnetodielectric with Disordered Magnetic and Electronic Ground States. *J. Magn. Magn. Mater.* **2018**, *466*, 354−358.

(12) Parant, C.; Bernier, J.-C.; Michel, A. Sur Deux Formes Orthorhombiques de Fe_2WO_6. *C. R. Acad. Sc. Paris Série C* **1973**, *276*, 495−497.

(13) Guskos, N.; Sadlowski, L.; Typek, J.; Likodimos, V.; Gamari-Seale, H.; Bojanowski, B.; Wabia, M.; Walczak, J.; Rychlowska-Himmel, I. Magnetic and EPR Studies of α-, β-, and γ-Fe_2WO_6 Phases at Low Temperatures. *J. Solid State Chem.* **1995**, *120* (2), 216−222.

(14) Guskos, N.; Likodimos, V.; Glenis, S.; Patapis, S. K.; Palilis, L. C.; Typek, J.; Wabia, M.; Rychlowska-Himmel, I. Electrical Transport and EPR Properties of the α, β, and γ Phases of Fe_2WO_6. *Phys. Rev. B: Condens. Matter Mater. Phys.* **1999**, *60* (11), 7687−7690.

(15) Walczak, J.; Rychiowska-Himmel, I.; Tabero, P. Iron(III) Tungstate and Its Modifications. *J. Mater. Sci.* **1992**, *27* (13), 3680−3684.

(16) Fauth, F.; Boer, R.; Gil-Ortiz, F.; Popescu, C.; Vallcorba, O.; Peral, I.; Fullà, D.; Benach, J.; Juanhuix, J. The Crystallography Stations at the Alba Synchrotron. *Eur. Phys. J. Plus* **2015**, *130* (8), 160.

(17) van der Linden, P. J. E. M.; Moretti Sala, M.; Henriquet, C.; Rossi, M.; Ohgushi, K.; Fauth, F.; Simonelli, L.; Marini, C.; Fraga, E.; Murray, C.; Potter, J.; Krisch, M. A Compact and Versatile Dynamic Flow Cryostat for Photon Science. *Rev. Sci. Instrum.* **2016**, *87* (11), 115103.

(18) Chapon, L. C.; Manuel, P.; Radaelli, P. G.; Benson, C.; Perrott, L.; Ansell, S.; Rhodes, N. J.; Raspino, D.; Duxbury, D.; Spill, E.; Norris, J. Wish: The New Powder and Single Crystal Magnetic Diffractometer on the Second Target Station. *Neutron News* **2011**, *22* (2), 22−25.

(19) Altomare, A.; Giacovazzo, C.; Guagliardi, A.; Moliterni, A. G. G.; Rizzi, R.; Werner, P.-E. New Techniques for Indexing: N-TREOR in EXPO. *J. Appl. Crystallogr.* **2000**, *33* (4), 1180−1186.

(20) Boultif, A.; Louer, D. Powder Pattern Indexing with the Dichotomy Method. *J. Appl. Crystallogr.* **2004**, *37* (5), 724−731.

(21) Palatinus, L.; Chapuis, G. SUPERFLIP - a Computer Program for the Solution of Crystal Structures by Charge Flipping in Arbitrary Dimensions. *J. Appl. Crystallogr.* **2007**, *40* (4), 786−790.

(22) Petříček, V.; Dušek, M.; Palatinus, L. Crystallographic Computing System JANA2006: General Features. *Z. Kristallogr. - Cryst. Mater.* **2014**, *229* (5), 345−352.

(23) Rodríguez-Carvajal, J. Recent Advances in Magnetic Structure Determination by Neutron Powder Diffraction. *Phys. B* **1993**, *192* (1−2), 55−69.

(24) Wells, A. F. Octahedral Structures. In *Structural Inorganic Chemistry*; Oxford University Press: London, 1975; pp 164−179.

(25) Shannon, R. D.; Prewitt, C. T. Effective Ionic Radii in Oxides and Fluorides. *Acta Crystallogr., Sect. B: Struct. Crystallogr. Cryst. Chem.* **1969**, *25* (5), 925−946.

(26) Almeida, M. A. P.; Cavalcante, L. S.; Morilla-Santos, C.; Filho, P. N. L.; Beltrán, A.; Andrés, J.; Gracia, L.; Longo, E. Electronic Structure and Magnetic Properties of $FeWO_4$ Nanocrystals Synthesized by the Microwave-Hydrothermal Method. *Mater. Charact.* **2012**, *73*, 124−129.

(27) Obermayer, H. A.; Dachs, H.; Schröcke, H. Investigations Concerning the Coexistence of Two Magnetic Phases in Mixed Crystals (Fe, Mn)WO_4. *Solid State Commun.* **1973**, *12* (8), 779−784.

(28) Kunnmann, W.; La Placa, S.; Corliss, L. M.; Hastings, J. M.; Banks, E. Magnetic Structures of the Ordered Trirutiles Cr_2WO_6, Cr_2TeO_6 and Fe_2TeO_6. *J. Phys. Chem. Solids* **1968**, *29* (8), 1359−1364.

(29) Ghara, S.; Suard, E.; Fauth, F.; Tran, T. T.; Halasyamani, P. S.; Iyo, A.; Rodríguez-Carvajal, J.; Sundaresan, A. Ordered Aeschynite-Type Polar Magnets $RFeWO_6$ (R = Dy, Eu, Tb, and Y): A New Family of Type-II Multiferroics. *Phys. Rev. B: Condens. Matter Mater. Phys.* **2017**, *95* (22), 1−11.

(30) Pearson, R. G. Concerning Jahn-Teller Effects. *Proc. Natl. Acad. Sci. U. S. A.* **1975**, *72* (6), 2104−2106.

(31) Kunz, M.; Brown, I. D. Out-of-Center Distortions around Octahedrally Coordinated d^0 Transition Metals. *J. Solid State Chem.* **1995**, *115* (2), 395−406.

(32) Halasyamani, P. S. Asymmetric Cation Coordination in Oxide Materials: Influence of Lone-Pair Cations on the Intra-Octahedral Distortion in d^0 Transition Metals. *Chem. Mater.* **2004**, *16* (19), 3586−3592.

(33) Ok, K. M.; Halasyamani, P. S.; Casanova, D.; Llunell, M.; Alemany, P.; Alvarez, S. Distortions in Octahedrally Coordinated d^0 Transition Metal Oxides: A Continuous Symmetry Measures Approach. *Chem. Mater.* **2006**, *18* (14), 3176−3183.

(34) Pauling, L. The Principles Determining the Structure of Complex Ionic Crystals. *J. Am. Chem. Soc.* **1929**, *51* (4), 1010−1026.

(35) Zhu, M.; Do, D.; Dela Cruz, C. R.; Dun, Z.; Zhou, H. D.; Mahanti, S. D.; Ke, X. Tuning the Magnetic Exchange via a Control of Orbital Hybridization in $Cr_2(Te_{1-x}W_x)O_6$. *Phys. Rev. Lett.* **2014**, *113* (7), 76406.

(36) Weingart, C.; Spaldin, N.; Bousquet, E. Noncollinear Magnetism and Single-Ion Anisotropy in Multiferroic Perovskites. *Phys. Rev. B: Condens. Matter Mater. Phys.* **2012**, *86* (9), 94413.

https://dx.doi.org/10.1021/acs.inorgchem.0c01024
Inorg. Chem. XXXX, XXX, XXX−XXX